APL Materials

RESEARCH ARTICLE | MAY 26 2026

Anisotropy-driven interfacial magnetism in Ru-deficient $SrRuO_3$ thin films

Special Collection: Low dimensionality effects in magnetic materials

V. A. de Oliveira Lima ; S. Nandi ; T. Brückel ; M. I. Faley ; O. Concepción ; A. Qdemat ; H. Ambaye ; V. Lauter ; M. Radovic ; A. Singh ; E. Kentzinger ; C. Bednarski-Meinke

Check for updates

APL Mater. 14, 051112 (2026)
https://doi.org/10.1063/5.0329378

View Online
Export Citation

Articles You May Be Interested In

Magnetic Properties of $SrRuO_3$ and $CaRuO_3$

J. Appl. Phys. (February 1968)

Metal-insulator transition in (111) $SrRuO_3$ ultrathin films

APL Mater. (September 2019)

Epitaxial integration and properties of $SrRuO_3$ on silicon

APL Mater. (August 2018)

28 May 2026 14:04:25

AIP Advances
Why Publish With Us?
21DAYS average time to 1st decision
OVER 4 MILLION views in the last year
INCLUSIVE scope
Learn More
AIP Publishing

AIP Publishing

Anisotropy-driven interfacial magnetism in Ru-deficient $SrRuO_3$ thin films

Cite as: APL Mater. 14, 051112 (2026); doi: 10.1063/5.0329378
Submitted: 17 February 2026 • Accepted: 8 May 2026 •
Published Online: 26 May 2026

View Online Export Citation CrossMark

V. A. de Oliveira Lima,[1,2,a] S. Nandi,[1,2] T. Brückel,[1,2] M. I. Faley,[3] O. Concepción,[4] A. Qdemat,[5] H. Ambaye,[5] V. Lauter,[5] M. Radovic,[6] A. Singh,[1] E. Kentzinger,[1] and C. Bednarski-Meinke[1,a]

AFFILIATIONS

[1] Jülich Centre for Neutron Science for Quantum Materials and Collective Phenomena (JCNS-2), Forschungszentrum Jülich GmbH, 52425 Jülich, Germany
[2] RWTH Aachen, Faculty of Mathematics, Computer Science and Natural Sciences, 52074 Aachen, Germany
[3] Ernst Ruska-Centre for Microscopy and Spectroscopy with Electrons (ER-C-1), Forschungszentrum Jülich GmbH, 52425 Jülich, Germany
[4] Peter Grünberg Institute for Semiconductor Nanoelectronics (PGI-9), Forschungszentrum Jülich GmbH, 52425 Jülich, Germany
[5] Neutron Scattering Division, Oak Ridge National Laboratory, Oak Ridge, Tennessee 37831, USA
[6] PSI Center for Photon Science, Paul Scherrer Institut, CH-5232 Villigen PSI, Switzerland

Note: This paper is part of the Special Topic on Low Dimensionality Effects in Magnetic Materials.
[a] **Authors to whom correspondence should be addressed:** v.de.oliveira.lima@fz-juelich.de and c.bednarski-meinke@fz-juelich.de

ABSTRACT

While stoichiometric $SrRuO_3$ (SRO) is a metallic itinerant ferromagnet with relatively homogeneous magnetization, Ru deficiency provides a powerful route to alter its electronic transport and depth-dependent magnetic properties. Ru-deficient SRO thin films grown by radio frequency high-oxygen pressure sputtering were investigated using a combination of x-ray reflectivity, polarized neutron reflectometry, off-specular neutron scattering, scanning transmission electron microscopy with energy-dispersive x-ray spectroscopy, electrical transport, and magnetometry. Structural and compositional analyses reveal that Ru deficiency is intrinsic to the films, with an enhanced deficiency at the interfaces. As a result, coherent electronic transport is suppressed and saturation magnetization is reduced, while the Curie temperature remains largely unaffected, placing Ru-deficient SRO in a regime consistent with ferromagnetic insulator-like behavior. Depth- and lateral-resolved magnetic measurements further indicate that the interfacial regions remain ferromagnetic, with a reduced in-plane magnetic projection consistent with enhanced perpendicular magnetic anisotropy that keeps the local magnetization predominantly out-of-plane. Our results establish Ru deficiency as a key control parameter governing transport, magnetization, and anisotropy in SRO thin films and highlight defect and interface engineering as powerful routes to tailor interfacial magnetism in correlated oxide heterostructures.

© 2026 Author(s). All article content, except where otherwise noted, is licensed under a Creative Commons Attribution (CC BY) license (https://creativecommons.org/licenses/by/4.0/). https://doi.org/10.1063/5.0329378

28 May 2026 14:04:25

I. INTRODUCTION

$SrRuO_3$ (SRO) is a complex transition metal oxide that has been used in ferroelectric tunnel junctions and as an electrode material due to its low room-temperature resistivity and high chemical and thermal stability.[1] Beyond these functional properties, SRO exhibits a wide range of rich and intriguing physical phenomena arising from strong coupling between charge, spin, and orbital degrees of freedom and the periodic crystal lattice. These interactions place SRO at the frontier of materials research for both conventional electronics and emerging quantum technologies.[2,3]

SRO stands out as a rare example of a 4*d* transition metal oxide that simultaneously exhibits itinerant ferromagnetism and metallic conductivity below its Curie temperature (T_{Curie}) of 160 K. More recently, it has attracted renewed interest as a platform for studying correlated and topological phenomena.[4–6] For instance, SRO

displays strain-tunable magnetic anisotropy with narrow domain walls, strong spin–orbit coupling, and unconventional transport behavior, including anomalous and topological Hall effects, linked to nontrivial Berry curvature.[5,7–9] Moreover, recent theoretical predictions suggest that SRO may host topological semimetal phases, such as Weyl points and Dirac nodal lines near the Fermi level.[10] Its physical properties are remarkably sensitive to epitaxial strain, dimensional confinement, interfacial effects, and film stoichiometry.[11–13]

Among these parameters, Ru deficiency plays a particularly important role in SRO thin films. Rather than acting as a simple source of disorder, Ru vacancies strongly modify the electronic bandwidth, magnetic exchange interactions, and magnetic anisotropy.[5,14–16] As a result, Ru-deficient SRO films can deviate substantially from the metallic itinerant ferromagnetic ground state of stoichiometric SRO, particularly at interfaces where stoichiometric disorder and anisotropy gradients are enhanced.[15,17] Wakabayashi *et al.* conducted a comparative study of the structural and electronic transport properties of stoichiometric and Ru-deficient SRO thin films grown by molecular beam epitaxy (MBE).[15] They observed two primary types of structural disorder in Ru-deficient films (Ru vacancies within the lattice and interface-driven disorders), which are thickness-dependent. These structural features were correlated with an enhanced magnetic moment, a reduction in T_{Curie}, and the suppression of the magnetic Weyl semimetal state.

In contrast, Mlynarczyk *et al.* investigated SRO films grown by direct current high oxygen pressure sputtering (DC-HOPS) and found that the Ru deficiency, ~14%, was localized at both film interfaces (i.e., at the surface and at the film–substrate interface), while the bulk of the film remained stoichiometric.[18] Despite the presence of Ru deficiency, the crystallinity of such films remains high, as evidenced by well-defined finite-thickness (Laue) oscillations in x-ray diffraction (XRD) measurements. The only notable difference between stoichiometric and Ru-deficient samples is a slight out-of-plane lattice expansion.[19] These observations highlight the complex nature of disorder in SRO thin films: even in the absence of major structural degradation, subtle modifications in stoichiometry can lead to significant changes in magnetic and electronic behavior.

In this work, we investigate Ru-deficient SRO thin films grown on Nb-doped and undoped $SrTiO_3$ substrates by radio frequency high oxygen pressure sputtering (RF-HOPS). Similar to the studies by Wakabayashi *et al.* and Mlynarczyk *et al.*, our films also exhibit signatures of Ru deficiency and interfacial inhomogeneity. While previous studies on such films have largely focused on transport properties and volume-averaged magnetic measurements, the impact of Ru deficiency on the depth-dependent magnetic structure, particularly at buried interfaces, remains poorly understood. Here, we address this issue by combining x-ray reflectivity and polarized neutron reflectometry to directly probe the nuclear and magnetic scattering length density profiles with nanometer resolution. Our approach provides new insights into how stoichiometry variations and interface quality affect the magnetic properties of Ru-deficient SRO thin films and is broadly relevant for defect-engineered control of interfacial magnetism in correlated oxide heterostructures.

II. EXPERIMENTAL DETAILS

Single-crystal Nb-doped (Nb:STO, 0.05 wt. % Nb, ≈0.1 at. %) and undoped $SrTiO_3$ (STO) (001) substrates, supplied by Shinkosha, with miscut angles ranging between 0.05° and 0.1°, were used for thin film growth. While undoped STO is a standard substrate for high-quality SRO thin films, it undergoes an antiferrodistortive (AFD) structural phase transition at ~105 K, which leads to the formation of structural domains and associated strain fields near the surface that can affect neutron scattering experiments and the magnetic response of adjacent thin films.[20] To avoid such effects, polarized neutron reflectometry and off-specular neutron scattering measurements were performed exclusively on films grown on Nb:STO substrates, for which Nb incorporation modifies the AFD transition temperature and domain formation behavior, reducing structural inhomogeneity at low temperatures.[21,22] Prior to deposition, all substrates were chemically etched using buffered HF and subsequently annealed at 950 °C for 2 h in air to obtain a well-defined TiO_2-terminated surface.[23]

The SRO thin films were deposited from a stoichiometric SRO target using RF-HOPS.[24–26] To guarantee high-quality thin film growth and an environment free of contaminants, the SRO target is pre-sputtered and the deposition chamber is pumped for 24 h before film deposition. The SRO thin film was deposited at T_{dep} = 785 °C using a target–substrate distance (D_{TS}) of 2.5 cm, oxygen pressure (P_{O_2}) of 1.5 mbar, and RF plasma generated using a forward power (FWDP) of 100 W. The SRO growth rate at such growth parameters is about 125 Å/h.[4]

The sample morphology and local roughness were analyzed using atomic force microscopy (AFM) in intermittent contact mode, employing an Agilent 5400 AFM/SPM system equipped with Mikromash HQ:NSC15 cantilevers. Epitaxial quality, layer thickness, and total surface roughness were examined through x-ray diffraction (XRD), x-ray reflectivity (XRR), reciprocal space mapping (RSM), and ϕ-scan measurements, conducted on a Rigaku SmartLab diffractometer. The crystal structure and the chemical composition across the film, with particular focus on the top and bottom interfaces, were investigated by high-angle annular dark-field (HAADF) scanning transmission electron microscopy coupled with energy-dispersive x-ray spectroscopy (STEM-EDS) using TFS Spectra 300 STEM and FEI Titan G2 80-200 ChemiSTEM.

Magnetic hysteresis and field-cooled magnetization measurements were performed as a function of temperature and applied magnetic field using a superconducting quantum interference device (SQUID) quantum design magnetic properties measurement system (MPMS-XL). The temperature dependence of the electrical transport properties was investigated by standard four-point probe resistivity measurements using a quantum design physical property measurement system (PPMS).

Polarized neutron reflectivity (PNR) and off-specular neutron scattering (OSS) were measured on the Magnetism Reflectometer, MAGREF,[27] at BL-4A of the Spallation Neutron Source, Oak Ridge National Laboratory, using a 10 × 10 mm^2 sample. Reflectivity was measured up to wave vector transfer ($\mathbf{Q_z}$) of 0.12 $Å^{-1}$ at 100, 80, and 5 K, following field cooling in a 4.8 T in-plane magnetic field (applied along the [100] crystallographic direction). The neutron spin polarization was set either parallel (R+) or antiparallel (R−) to the field direction and was applied throughout the measurements.

28 May 2026 14:04:25

© Author(s) 2026

III. RESULTS AND DISCUSSION

Unless otherwise stated, the structural and magnetic results presented in this section refer to Ru-deficient SRO films grown on Nb:STO substrates, which were selected for neutron scattering experiments to avoid substrate-related structural artifacts. The Nb:STO substrate exhibits the characteristic terraced morphology associated with TiO_2 surface termination [Fig. 1(a)]. Its root mean square (RMS) local roughness calculated from $5 \times 5\ \mu m^2$ AFM scans is ~8 ± 2 Å.

The morphology of the deposited 375 Å (determined from the calibrated SRO growth rate) SRO thin film [Fig. 1(b)] reveals evidence of a Stranski–Krastanov growth mode (layer-plus-island growth), as indicated by the presence of multiterraced islands. Such growth behavior may be influenced by several factors, including the substrate miscut angle,[23,28] the terraces alignment in relation to the [010] substrate direction (also called the angle of miscut direction),[23,29,30] and the substrate surface energy.[31] Figure 1(c) shows a magnified view of the region marked in Fig. 1(b), emphasizing the contours of a multiterraced island. The presence of multiple concentric terraces surrounding an individual island nucleus suggests that secondary nucleation occurs on top of preexisting islands. Importantly, the island morphology appears largely isotropic in the plane of the film, indicating that the directional information associated with the substrate step edges is not preserved during growth. As a consequence, any step-edge-induced anisotropy is strongly

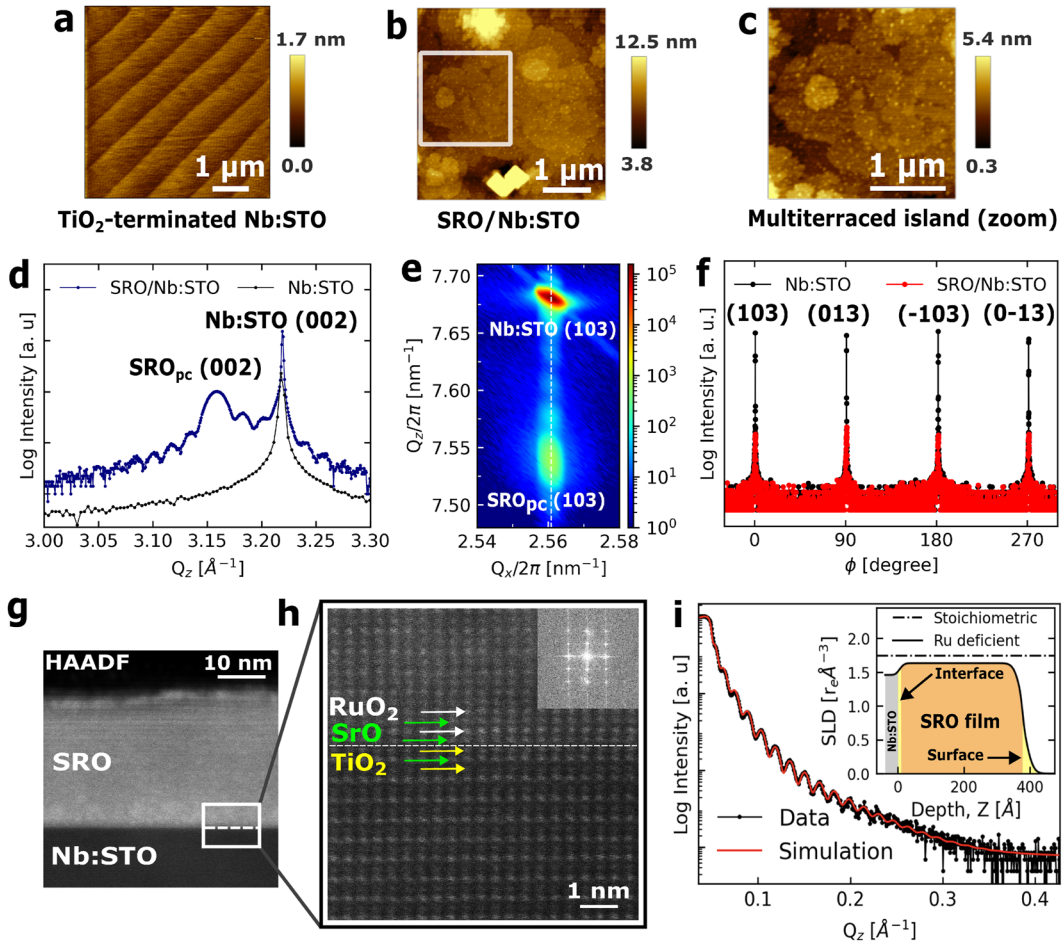

FIG. 1. Atomic force microscopy micrographs of (a) the Nb:STO substrate and (b) the SRO thin film grown on Nb:STO. (c) Magnified view of the highlighted region in panel (b). The magnified image highlights the concentric multi-terraced structure of an individual island. (d) X-ray diffraction pattern showing clear Laue oscillations, indicating the high crystalline quality of the SRO film. (e) Reciprocal space map and (f) ϕ-scans measured around the (103) crystallographic reflection of the SRO thin film and Nb:STO substrate. (g) Cross-sectional high-angle annular dark-field scanning transmission electron microscopy (HAADF-STEM) image of the epitaxial SRO film on the Nb:STO substrate. (h) Atomic-resolution image of the interface, revealing a sharp transition with alternating RuO_2/SrO/TiO_2 planes; the white dashed line marks the position of the SRO/Nb:STO interface. The inset shows the fast Fourier transform of the atomic-resolution image. (i) X-ray reflectivity data (black symbols) and corresponding GenX simulations (red line) based on a structural model that includes reduced scattering length density (SLD) layers at both the surface and the buried interface (SRO/Nb:STO). The inset shows the real part of the extracted SLD depth profile. The dashed–dotted horizontal line indicates the nominal x-ray SLD expected for stoichiometric SRO, shown as a reference.

28 May 2026 14:04:25

© Author(s) 2026

reduced in the SRO layer. This isotropic island growth and relatively high roughness are consistent with the coexistence of multiple in-plane crystallographic domain variants. The RMS local roughness of the SRO film, calculated over an area of 2.5 × 2.5 μm^2, was 37 ± 14 Å.

The high crystalline quality of the SRO thin film is evidenced by the presence of Laue oscillations in the XRD pattern [Fig. 1(d)]. The film shows epitaxial growth, with an in-plane lattice parameter that is compressed and aligned with that of the substrate, as confirmed by the RSM and ϕ-scans performed around the pseudocubic (103) crystallographic reflection of the SRO thin film and Nb:STO substrate [Figs. 1(e) and 1(f)]. The out-of-plane lattice parameter obtained from the RSM (3.98 ± 0.02 Å), which is larger than that for stoichiometric SRO films (3.949 Å), provides a first indication of Ru deficiency in the film.[15,19] The in-plane crystallographic structure was further examined by ϕ-scan measurements around the SRO_{pc} (103) reflection [Fig. 1(f)]. The ϕ-scan reveals four well-defined peaks separated by 90°, evidencing the coexistence of two in-plane orthorhombic (110) domain variants. The comparable peak intensities indicate similar domain populations, consistent with previous reports on SRO films grown on exact or low-miscut TiO_2-terminated STO substrates.[29,32] Such multidomain growth is commonly observed when no dominant step-edge anisotropy is imposed by the substrate, in agreement with the isotropic island morphology observed by AFM.

Cross-sectional high-angle annular dark-field scanning transmission electron microscopy (HAADF-STEM) reveals a fully epitaxial SRO film grown on Nb:STO with a coherent and atomically sharp interface, confirming the high crystalline quality of the heterostructure [Fig. 1(g)]. The atomic-resolution image in Fig. 1(h) clearly shows the alternating RuO_2, SrO, and TiO_2 planes, indicative of an ordered perovskite stacking across the interface. The white dashed line marks the position of the SRO/Nb:STO interface. The inset in Fig. 1(h) shows the fast Fourier transform (FFT) of the atomic-resolution image, confirming the high degree of crystallinity and epitaxial coherence. It is worth noting that, at the Ru deficiency levels inferred from compositional analyses, the perovskite stacking remains intact and structural signatures of Ru vacancies are not directly discernible in atomic-resolution HAADF-STEM images, which primarily probe the local structural order.

To quantitatively determine the total film thickness (t) and interfacial roughness (σ), XRR data were analyzed using GenX software.[33] Several structural models, based on stacked block-like layers on a substrate, were implemented to represent the layered architecture of the film. A schematic overview of these models, along with their key parameters, is provided in the supplementary material (Sec. S1). While all tested models successfully reproduced the overall periodicity of the XRR oscillations (supplementary material, Sec. S2), primarily sensitive to the film thickness and interfaces, only one model (model 4) adequately captures the finer features associated with interfacial roughness. This model includes reduced scattering length density (SLD) interfaces at both the top (surface) and bottom (SRO-Nb:STO) film boundaries. The experimental XRR pattern and the corresponding simulation are shown in Fig. 1(i).

The total film thickness is t = 382 ± 3 Å, corresponding to the sum of all sublayer thicknesses and consistent with the expected thickness based on the calibrated SRO growth rate. In contrast to the total geometrical thickness obtained from XRR, the finite-thickness (Laue) oscillations observed around the SRO_{pc} (002) reflection yield a structurally coherent crystalline thickness of t_{coh} = 255 ± 6 Å. The smaller coherent thickness compared to the XRR-derived value reflects the distinct physical quantities accessed by the two techniques: while XRR is sensitive to the full electron density profile, including chemically and structurally modified surface and SRO/Nb:STO interface regions, Laue oscillations arise only from the coherently ordered fraction of the film. In Ru-deficient SRO, vacancy-induced disorder and strain inhomogeneities are expected to reduce the out-of-plane coherence length, consistent with the vacancy-driven structural degradation discussed in Ref. 15.

The roughness parameters extracted for the substrate/film interface, internal film interfaces, and the film surface were σ = 10, 5, and 21 Å, respectively. Assuming uncorrelated interfaces, these values yield an average effective interfacial roughness of $\sigma_{eff} \approx 13.7 \pm 2$ Å, estimated by an RMS combination of the individual roughness parameters. This assumption is physically justified by the different origins of roughness at the substrate and film interfaces: substrate roughness is dominated by step–terrace structures associated with the miscut, whereas film roughness arises from growth-induced morphology and island coalescence, leading to largely independent height fluctuations.

The thicknesses of the surface and SRO–STO interface regions are estimated to be in the ranges of 4–10 and 10–30 Å, respectively, in good agreement with values reported by Mlynarczyk *et al.*[17,18] In those studies, Ru deficiency was found to be concentrated at both the top and bottom interfaces of the film, leading to Sr enrichment in these regions, while the bulk of the film remained stoichiometric.[18] Here, our XRR results provide a quantitative structural signature of this compositional variation by revealing a reduced x-ray SLD at the interfaces. Moreover, Ru deficiency is not confined to the interfaces but extends throughout the entire film thickness, as evidenced by the reduced SLD in the central region (1.633 ± 0.024 $r_e Å^{-3}$) compared to the theoretical x-ray SLD of stoichiometric SRO (1.746 $r_e Å^{-3}$), as indicated by the dashed–dotted horizontal line [see inset of Fig. 1(i)]. Assuming constant atomic density and full oxygen stoichiometry, the reduced x-ray SLD corresponds to an effective Ru deficiency of 24%, providing an upper bound for the Ru vacancy concentration (supplementary material, Sec. S3).

This interpretation is further supported by Rutherford backscattering spectroscopy (RBS) measurements. Figure 2(a) shows the RBS spectrum of the SRO/Nb:STO film together with RUMP simulations using two representative compositions: stoichiometric $SrRuO_3$ and a Ru-deficient model ($SrRu_{0.75}O_3$). The Ru content predominantly affects the feature around ~1.1 MeV and the high-energy shoulder of the Ru signal, for which the Ru-deficient model provides a significantly improved agreement with the experimental spectrum. This indicates that the film is globally Ru-poor, with an effective Ru deficiency on the order of ~20%–25%. We note that as a depth-integrated and heavy-element-weighted technique under the present measurement conditions, RBS primarily constrains the overall cation stoichiometry and is comparatively less sensitive to interfacial composition gradients and oxygen non-stoichiometry.

To obtain spatially resolved compositional information and directly probe interfacial chemical gradients, STEM-EDS was performed in the cross-sectional region [Fig. 2(b)]. Elemental maps for

28 May 2026 14:04:25

© Author(s) 2026

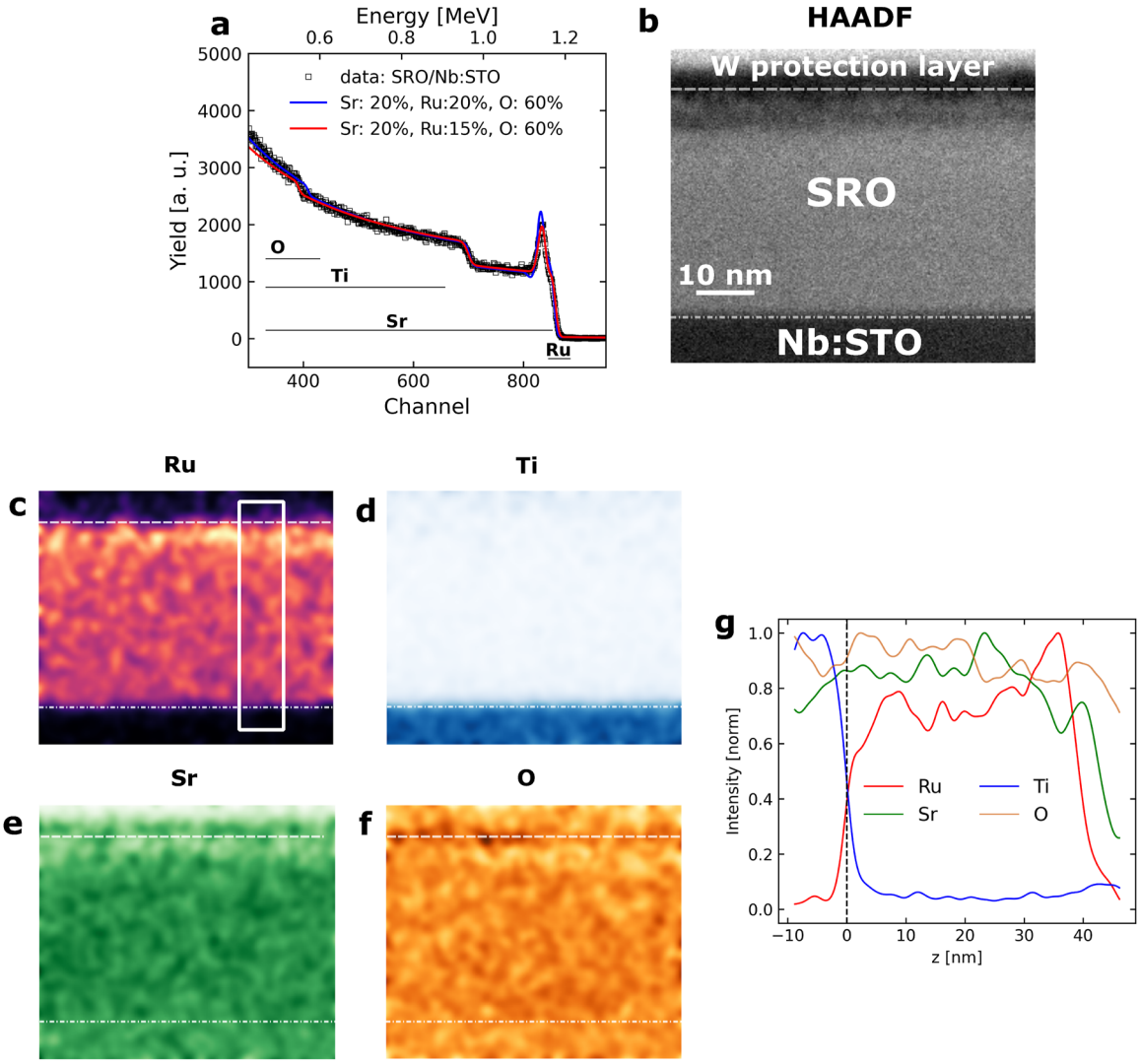

FIG. 2. (a) Rutherford backscattering spectroscopy spectrum of the SRO/Nb:STO thin film together with RUMP simulations assuming stoichiometric $SrRuO_3$ (blue line) and a Ru-deficient composition ($SrRu_{0.75}O_3$, red line). (b) Cross-sectional HAADF-STEM image of the region used for compositional mapping. (c)–(f) Corresponding STEM-EDS elemental maps of Ru, Ti, Sr, and O, respectively. The dashed lines in panels (c)–(f) are guides to the eye, marking the approximate positions of the film surface and the buried SRO/Nb:STO interface. (g) Laterally integrated and normalized STEM-EDS intensity profiles extracted from the region indicated in panel (c), plotted as a function of depth z, where $z = 0$ corresponds to the SRO/Nb:STO interface.

Ru, Ti, Sr, and O are presented in Figs. 2(c)–2(f). Laterally integrated STEM-EDS intensity profiles are shown in Fig. 2(g) to facilitate a direct comparison of the depth-dependent elemental distributions across the sample. The profiles were extracted from the region indicated in Fig. 2(c) and are plotted as a function of depth using the same convention adopted in the x-ray and neutron reflectometry analyses, with the SRO/Nb:STO interface defined as $z = 0$.

The Ru map reveals pronounced compositional gradients, with reduced Ru signal near both the film surface and the buried SRO/Nb:STO interface, qualitatively consistent with the reduced SLD layers inferred from XRR. The Ru depletion appears stronger at the buried interface than near the surface, suggesting that Ru deficiency is enhanced at the substrate side. In addition, a slight Ru enhancement is observed in the subsurface region, indicating a non-uniform Ru distribution across the film thickness. Although the nominal growth parameters were kept constant during deposition, chemically non-uniform incorporation may still occur in SRO under high-temperature oxidizing growth conditions. Previous studies on SRO epitaxy have shown that the growth surface can be chemically dynamic, with termination-dependent surface diffusion and growth-mode evolution.[34] In addition, preferential Ru loss under oxidizing conditions has been discussed in the literature in

28 May 2026 14:04:25

© Author(s) 2026

terms of volatile Ru-oxide formation, particularly RuO_3 and RuO_4, at elevated temperature and oxygen partial pressure.[16–18,35] Within this framework, the near-surface compositional inhomogeneity may reflect the combined effects of preferential Ru loss at the film surface, local redistribution during growth, and post-growth reorganization during cooling and oxidation. Quantitative interpretation remains limited by the spatial resolution and thickness integration of the EDS measurement.

The Ti map shows no clear evidence of Ti diffusion into the SRO layer (within the sensitivity of STEM-EDS), supporting chemically well-defined interfaces. The Sr and O maps exhibit comparatively weaker variations; regions of reduced Ru signal tend to coincide with a slight relative Sr enhancement, consistent with local cation redistribution and relative off-stoichiometry. A fully quantitative description would additionally require assessing possible oxygen non-stoichiometry, which is not robustly constrained by the present RBS/EDS data. The combined RBS and STEM-EDS results corroborate the XRR-based structural model and support a picture of Ru deficiency that is enhanced at interfaces and present throughout the film.

The high volatility of Ru can lead to the formation of distinct types of Ru-vacancy-related disorder, as identified by Wakabayashi *et al.*[15] One contribution arises from Ru vacancies distributed throughout the bulk of the film, introducing structural disorder that can reduce the coherent crystalline thickness relative to the total thickness measured by XRR. A second contribution is interface-driven disorder, associated with compositional and structural variations localized at the film–substrate interface, which can influence the interfacial quality and the depth-dependent SLD profile. In this context, XRR provides the quantitative link between the depth-integrated stoichiometry obtained from RBS and the local compositional variations revealed by STEM-EDS, yielding a statistically averaged depth profile of Ru deficiency across the film. This combined structural and compositional picture establishes a consistent physical framework for understanding the properties of Ru-deficient SRO.

Electron transport properties are strongly affected by Ru deficiency, as evidenced by the temperature dependence of the resistivity [Fig. 3(a)] for films grown on both Nb-doped and undoped STO substrates. The absence of a discernible kink at the Curie temperature ($T_{Curie} \approx 160$ K) and the pronounced increase in resistivity at low temperatures indicate semiconducting or insulating behavior within the measured temperature range. The insulating response observed for the film grown on the undoped STO substrate demonstrates that the Ru-deficient SRO layer itself is intrinsically non-metallic, consistent with previous reports on Ru-poor SRO thin films.[15] For the film grown on the Nb-doped substrate, the resistivity curve exhibits apparent metallic-like temperature dependence. However, this behavior is dominated by a shunting effect, whereby the electrical current preferentially flows through the highly conductive Nb:STO substrate rather than through the SRO layer. As a result, the measured resistivity underestimates the intrinsic resistivity of the Ru-deficient SRO film, as it includes a substantial contribution from the conductive substrate. This decoupling between electronic transport and magnetic order reflects the sensitivity of Ru–O–Ru hopping to vacancy disorder, while the ferromagnetic exchange interaction remains comparatively robust.

The temperature dependence of the magnetization $M(T)$, measured after field cooling the sample in a magnetic field of 50 Oe applied perpendicular (out-of-plane) and parallel (in-plane) to the film surface, is shown in Fig. 3(b). The T_{Curie} value of 158.6 ± 0.5 K was extracted from the first derivative of the FC data [inset of Fig. 3(b)]. Complementary magnetization measurements performed on Ru-deficient SRO films grown on undoped STO substrates are provided in the supplementary material (Sec. S5, Fig. S3). The T_{Curie} value is not strongly affected by the Ru deficiency in SRO films prepared by RF-HOPS, which contrasts with T_{Curie} values of Ru-poor SRO films prepared by MBE (~140 K) and pulsed laser deposition (~143 K), where similar levels of non-stoichiometry have been reported to lower T_{Curie}.[15,36] These observations highlight the distinct behavior of SRO films grown by RF-HOPS, suggesting that this technique not only influences the spatial distribution of Ru vacancies but also may mitigate their detrimental effects on magnetic ordering. This combination of non-metallic transport behavior and a robust T_{Curie} is consistent with a ferromagnetic insulator-like regime induced by Ru-vacancy-related disorder.

In addition to the ferromagnetic transition, a distinct feature emerges in FC magnetization below T_{Curie}, starting at ~117 K and peaking near 87 K. This temperature range coincides with the AFD cubic-to-tetragonal structural transition of the STO substrate, which typically occurs between 110 and 65 K.[20] Simultaneously, a clear bifurcation between the out-of-plane and in-plane magnetization components develops in Fig. 3(b), consistent with an enhancement of perpendicular magnetic anisotropy (PMA) upon cooling. The persistence of this feature suggests that Nb doping does not suppress the AFD transition, but rather modifies its onset temperature and domain configuration,[21,22] potentially influencing the magnetic anisotropy of the adjacent Ru-deficient SRO film. At the same time, given the pronounced depth-dependent Ru deficiency of the film, an additional contribution from film-intrinsic variations in magnetic response and anisotropy across the thickness cannot be excluded.

The temperature evolution of the magnetic anisotropy is further elucidated by the magnetic hysteresis loops $M(H)$, as shown in Figs. 3(c)–3(g). All hysteresis loops were recorded after field cooling under an applied magnetic field of 5 T. At 135 K and 120 K [Figs. 3(c) and 3(d)], the out-of-plane (OP) and in-plane (IP) $M(H)$ are nearly identical, indicating only weak PMA in this temperature range. Upon further cooling to 100 K [Fig. 3(e)], a clear bifurcation between the OP and IP magnetization emerges, marking a crossover toward enhanced PMA. This crossover temperature coincides with the onset of the OP–IP separation observed in the FC $M(T)$ [Fig. 3(b)]. At lower temperatures, 80 and 5 K [Figs. 3(f) and 3(g)], the anisotropy becomes pronounced, with the OP direction acting as a clear easy axis, characterized by sharp magnetization reversal and easier saturation compared to the IP hard axis. The progressive enhancement of PMA upon cooling suggests that structural and interfacial effects, potentially amplified by the AFD transition of the Nb:STO substrate, may play an important role in stabilizing the magnetic anisotropy in Ru-deficient SRO films.

At the lowest temperatures, additional features appear in the hysteresis loops, most notably small irregularities in the magnetization reversal, particularly at 5 K. Such step-like features are characteristic of multidomain behavior commonly observed in strained

28 May 2026 14:04:25

© Author(s) 2026

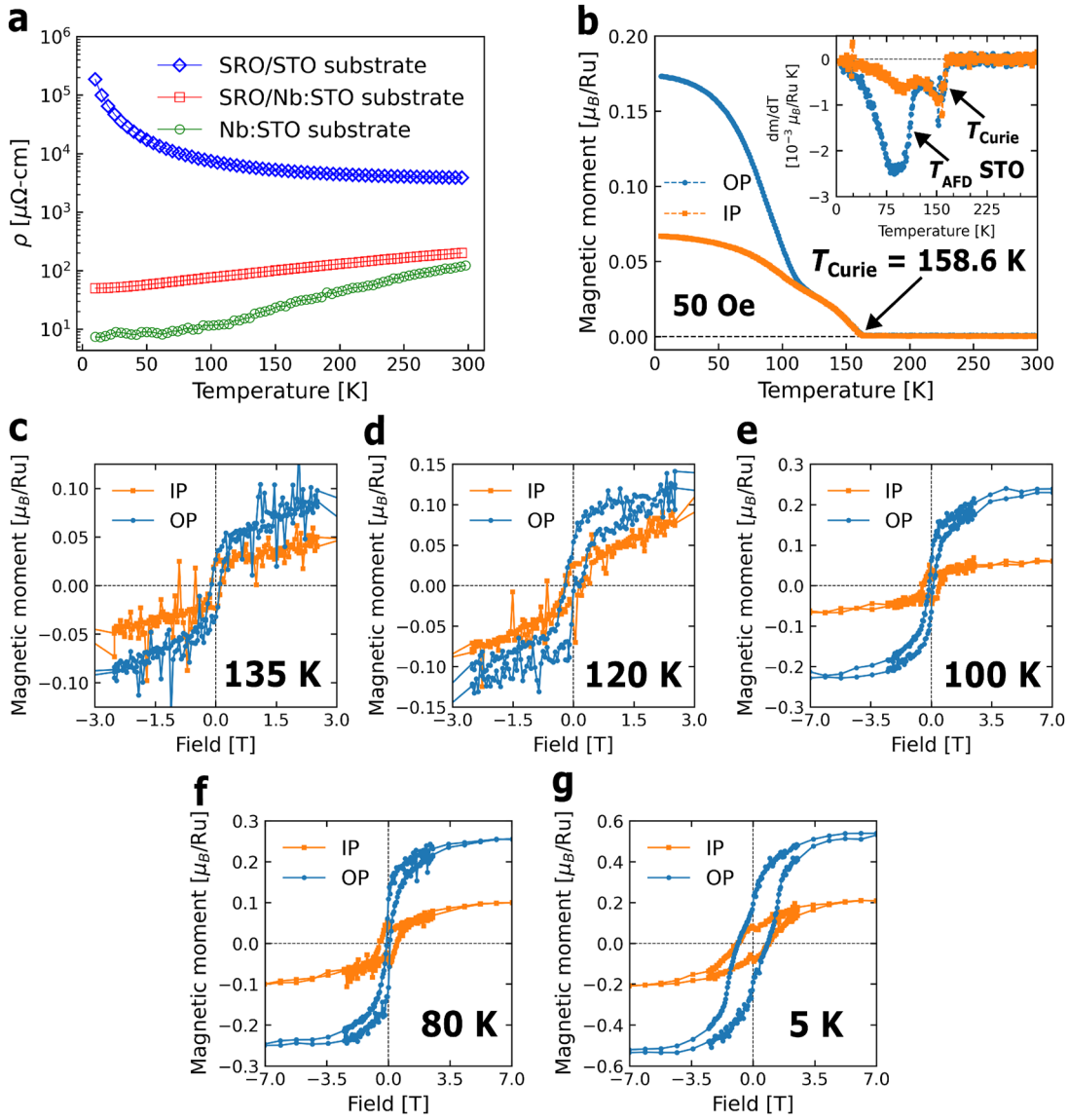

FIG. 3. (a) Temperature dependence of the resistivity for SRO thin films grown on undoped STO and Nb-doped STO substrates. (b) Field-cooled magnetization measured under an applied field of 50 Oe, with the field oriented perpendicular (out-of-plane, OP) and parallel (in-plane, IP) to the film surface. The inset shows the first derivative of the magnetization, highlighting the Curie temperature (T_{Curie}) and the antiferrodistortive transition temperature (T_{AFD}) of the STO substrate. (c) and (d) Magnetic hysteresis loops M(H) measured at 135 and 120 K, respectively, showing weak perpendicular magnetic anisotropy (PMA) with nearly identical OP and IP responses. (e) M(H) measured at 100 K, revealing the onset of a clear bifurcation between OP and IP magnetization, indicative of a crossover toward enhanced PMA. (f) and (g) M(H) measured at 80 and 5 K, respectively, displaying a pronounced enhancement of PMA, with easier saturation along the OP direction. For clarity, the hysteresis loops at 135 and 120 K are shown up to 3 T due to increased noise at higher fields. All M(H) were performed after field cooling the sample in 5 T.

SRO thin films.[29,32] In this regime, multiple crystallographic and magnetic domain variants can coexist, giving rise to non-smooth magnetization reversal processes.[9,30,37] These multidomain states are consistent with terrace-induced IP variants arising from the low substrate miscut and terrace orientation. In the present Ru-deficient film, this low-temperature behavior may additionally reflect the fact that different parts of the film thickness may not respond identically because of the depth-dependent composition and anisotropy.

In stoichiometric SRO, the OP saturation magnetic moment per Ru atom typically reaches about 1.6 μ_B at low temperatures.[16] In contrast, the present Ru-deficient film exhibits a significantly reduced effective magnetic moment of ~0.53 μ_B/Ru at 5 K. This value was obtained by normalizing the SQUID magnetization to

28 May 2026 14:04:25

© Author(s) 2026

the effective magnetic moment per Ru atom following the procedure described in the supplementary material (Sec. S6). This normalization is used as a convenient way to compare the effective magnetic moment with literature values expressed in μ_B/Ru and should not be interpreted as a site-specific attribution of the entire magnetic moment exclusively to Ru. This reduction is consistent with a weakening of the Ru–O–Ru exchange interactions that mediate ferromagnetism in SRO,[16] as Ru vacancies locally break these exchange paths, introducing magnetic frustration and weakening the double-exchange mechanism responsible for long-range order.[15,38] Nevertheless, the persistence of a robust ferromagnetic signal indicates that the vacancy concentration remains below the threshold that would fully suppress magnetic ordering.

The high-field saturation magnetization also shows a clear dependence on the direction of the applied magnetic field, a behavior commonly reported for SRO thin films. Several factors may contribute to this anisotropic response.[39] Ziese *et al.* noted that the typical procedure for subtracting the diamagnetic substrate background, which is done by removing the extrapolated high-field slope, may neglect paramagnetic contributions from the film itself, potentially leading to incorrect estimates of the saturation magnetization along different crystallographic directions.[40] Moreover, the anisotropy field in SRO can exceed the maximum applied magnetic field, thereby preventing full saturation magnetization along the magnetic hard axes.[16] Structural defects may also contribute to the suppression of full saturation by disrupting magnetic order.[37]

The SQUID magnetization curves (Fig. 3) provide values directly proportional to the total volume magnetization of the sample and, as such, do not offer the spatial resolution necessary to probe interface-specific magnetic behavior. In contrast, PNR provides depth-resolved information on both the nuclear and magnetic structures of thin films and buried interfaces.[41,42] The nuclear scattering length density (nSLD) describes the atomic structure, whereas the magnetic scattering length density (mSLD) reflects the IP component of the magnetization as a function of depth.[41–45] It, therefore, represents the effective magnetic contribution to the neutron magnetic scattering, rather than a site-specific decomposition into separate Ru and O moments. This distinction is particularly relevant in SRO, where the magnetic response arises from the hybridized Ru–O electronic network, and oxygen is known to carry a significant fraction of the total magnetic moment.[46,47]

To investigate the influence of Ru deficiency on the magnetic depth profile of SRO thin films, PNR measurements were performed at selected temperatures following field cooling in a 4.8 T magnetic field applied parallel to the film surface (IP). During the measurements, the magnetic field remained applied IP and the neutron spin polarization was set parallel (R+) or antiparallel (R−) to this direction, corresponding to the IP [100] axis, which represents the magnetic hard axis of the film. In this configuration, the neutron spin is sensitive to the IP component of the effective magnetization, allowing the separation of the nuclear and magnetic SLD profiles. The applied field of 4.8 T corresponds to the maximum available at the instrument and remains well below the reported anisotropy

28 May 2026 14:04:25

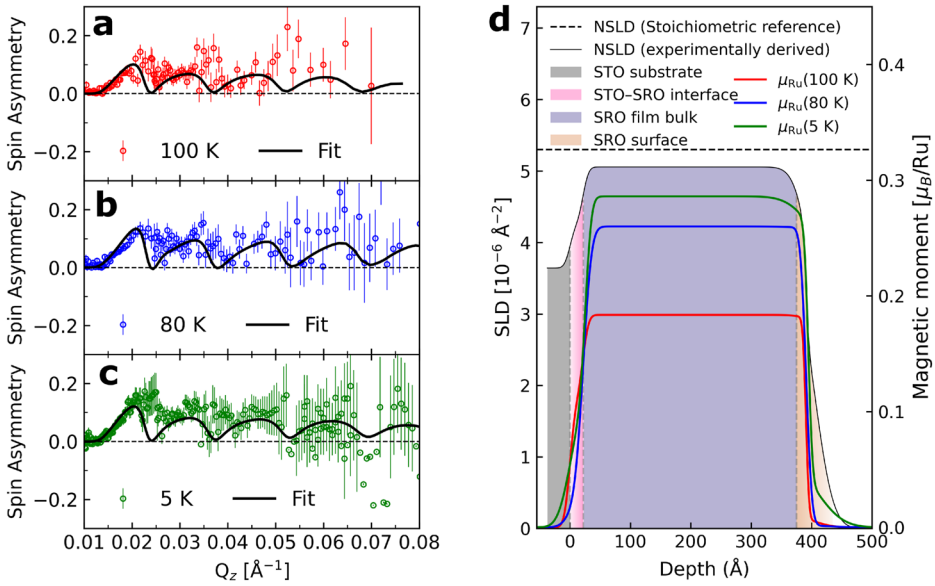

FIG. 4. (a)–(c) Spin asymmetry [(R+) − (R−)]/[(R+) + (R−)] measured at (a) 100 K, (b) 80 K, and (c) 5 K after field cooling the sample in a 4.8 T in-plane magnetic field. The open symbols represent the experimental data, and the solid lines represent the fits obtained from the best-refined model. (d) Nuclear scattering length density (nSLD, left axis) and magnetization profiles (right axis) derived from the magnetic scattering length density (mSLD) extracted from the fits. The dashed line indicates the nominal nuclear SLD expected for stoichiometric bulk $SrRuO_3$. The reduced nSLD relative to the reference value indicates Ru deficiency extending throughout the film thickness. The interfacial regions at the film surface and at the SRO/STO interface, where the nSLD is further reduced and consistent with enhanced Ru deficiency, are highlighted by the shaded areas. The magnetization profiles reveal finite magnetization at all temperatures, with reduced values in these interfacial regions compared to the film bulk.

© Author(s) 2026

field of SRO along the hard axis (12–14 T),[16] such that the film is not fully saturated in this direction. PNR measurements were performed at 100, 80, and 5 K, corresponding to representative temperatures selected based on the magnetometry results.

Figures 4(a)–4(c) shows the experimental spin asymmetry [(R+) − (R−)]/[(R+) + (R−)] curves together with the corresponding fits. The use of spin asymmetry emphasizes the magnetic contribution to the reflectivity by removing the purely structural background. The oscillatory behavior observed at 100, 80, and 5 K indicates a finite magnetic contrast within the film, which increases slightly upon cooling. Although the amplitude of the spin asymmetry is small, consistent with the weak in-plane magnetic contrast of Ru-deficient SRO in the present measurement geometry, it is sufficient to extract reliable depth-dependent magnetization profiles.

The corresponding nSLD and magnetization profiles obtained from the fits are shown in Fig. 4(d). The magnetization profiles were derived from the mSLD obtained in the PNR fits, following the procedure described in the supplementary material (Sec. S6). The structural parameters extracted from PNR, including the film thickness and interface roughness, are in good agreement with those derived from XRR and AFM analyses, confirming the internal consistency of the structural model. Complementary to the XRR results, the PNR data indicate that the reduced nSLD is not confined to the interfaces but extends throughout the entire film thickness, consistent with Ru deficiency across the film thickness and resulting in a uniformly reduced nSLD compared to the stoichiometric value [dashed line in Fig. 4(d)]. A quantitative comparison between the nSLD obtained from PNR and the x-ray-derived SLD further supports this consistency (supplementary material, Sec. S4). Notably, the nSLD profiles exhibit further reductions in the interfacial regions, which appear as lighter shaded areas in Fig. 4(d). These regions coincide with the interfaces identified by XRR and STEM-EDS and are, therefore, consistent with an enhanced Ru deficiency near both the film surface and the buried SRO/STO interface.

From the magnetic point of view, the film retains a finite magnetic signal across all temperatures, as shown by the magnetization profiles in Fig. 4(d). Here, the magnetization profiles represent the in-plane component probed by PNR. The interface regions also exhibit measurable magnetic signals, although significantly reduced relative to the film bulk. For quantitative comparison with SQUID magnetometry, the depth-resolved magnetization profiles obtained from PNR were normalized to an effective magnetic moment per Ru atom (μ_B/Ru), following the procedure described in the supplementary material (Sec. S6). This normalization is used for comparison with literature values expressed in μ_B/Ru and does not imply that the magnetic moment is exclusively localized on Ru. The average magnetic moment values extracted from PNR ($\langle\mu\rangle$ = 0.18, 0.26, and 0.29 μ_B/Ru at 100, 80, and 5 K, respectively) were calculated as a thickness-weighted mean of the layer magnetizations according to $\langle\mu\rangle = \sum_i \mu_i t_i / \sum_i t_i$, where t_i and μ_i are the thickness and magnetization of each layer, respectively. This procedure yields a thickness-weighted average in-plane magnetic moment per Ru, directly comparable with the SQUID values expressed in μ_B/Ru.

The obtained values fall between the IP and OP SQUID magnetization components: at 100 and 80 K, the PNR magnetization is closer to the OP SQUID values, while at 5 K, it approaches the IP component. This evolution is consistent with a gradual rotation of the effective magnetization toward the film plane under field cooling in 4.8 T, although complete IP alignment is not achieved. The small amplitude of the spin-asymmetry signal and the lack of full IP saturation further support the presence of a significant OP component stabilized by the strong PMA. The strong PMA observed in SQUID magnetometry independently indicates that the reduced in-plane magnetization detected by PNR at the interfaces is more naturally interpreted as a suppression of the in-plane projection rather than a complete loss of magnetic order. Within this framework, the PNR results are consistent with a partially canted magnetic configuration that evolves upon cooling under an IP applied field. In a film with depth-dependent Ru deficiency, such behavior may also reflect a depth-dependent magnetic configuration arising from local variations in composition and PMA across the film thickness, rather than a rigid rotation of a single uniform magnetization vector. All SQUID and PNR measurements discussed here were performed following the same field-cooling protocol. Therefore, the observed evolution can be discussed in terms of intrinsic changes in the magnetic configuration under equivalent preparation conditions.

Figure 5 shows the OSS maps acquired at 100, 80, and 5 K for both spin channels (R+ and R−). The maps display the expected central specular line at $K_{i_z} - K_{f} = 0$ and diffuse scattering along the diagonal directions, characteristic of lateral structural or magnetic roughness and interfacial inhomogeneity, called Yoneda scattering.[41,48,49] The scattering arises from refraction and enhancement of the scattered waves at the surface and interface of a material, particularly when the angle of the scattered waves is close to the critical angle of the film. Upon cooling, the diffuse magnetic scattering becomes more pronounced. Here, this evolution is discussed in terms of a relative redistribution of the diffuse scattering intensity since the maps are background-subtracted and compared using the same color scale.

The OSS results provide complementary qualitative evidence supporting the depth-resolved magnetic profiles obtained from PNR. The enhanced diffuse scattering at low temperature is consistent with changes in the magnetic configuration under the applied IP field, within a picture where strong PMA preserves a finite OP magnetization component while the applied field favors an increasing IP projection upon cooling. In a film with depth-dependent Ru deficiency, this behavior may also be associated with a magnetic configuration that varies both in thickness and laterally, leading to modified magnetic correlations and a redistribution of the diffuse scattering intensity. Within the present experimental sensitivity, the OSS data, therefore, qualitatively support the PNR-based interpretation that the magnetization does not rotate rigidly into the film plane, but instead evolves toward a partially canted state at low temperature.

Simulated OSS maps [Figs. 5(g) and 5(h)], performed according to Refs. 50 and 51 using the structural and magnetic parameters extracted from the 5 K PNR fits, capture the main experimental features, including the diagonal diffuse bands. This agreement indicates that the structural and magnetic roughness of the film and substrate are largely uncorrelated, consistent with island-like growth on TiO_2-terminated Nb:STO substrates. The analysis further suggests that within the present experimental sensitivity, the lateral magnetic roughness closely follows the nuclear roughness profile, while the

28 May 2026 14:04:25

© Author(s) 2026

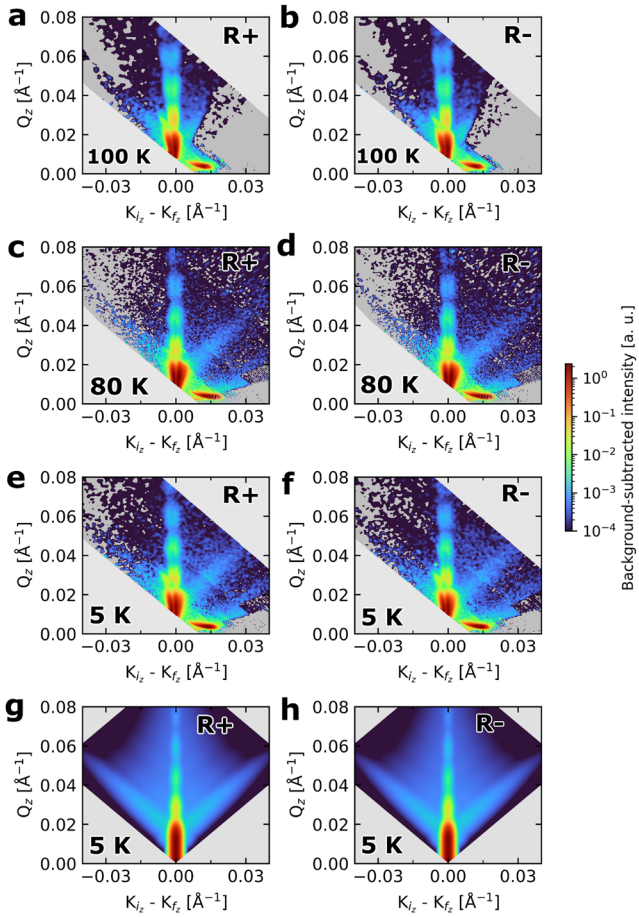

FIG. 5. Polarized off-specular neutron scattering (OSS) maps measured at 100, 80, and 5 K for both spin channels R+ (a), (c), and (e) and R− (b), (d), and (f), after field cooling in a 4.8 T in-plane magnetic field. The intensities were background-subtracted, and the same color scale is used for all temperatures to facilitate comparison of relative changes in the scattering distribution. The light-gray regions indicate areas outside the physical scan area, while the darker-gray regions correspond to measured parts of the scan where no intensity values are displayed after background subtraction and intensity cutoff. Panels (g) and (h) show simulated OSS patterns calculated from the PNR-derived structural and magnetic parameters at 5 K, capturing the main experimental features.

reduced magnetic response of the Ru-deficient SRO film limits the overall magnetic contrast.

Given the substantial reduction in interfacial magnetization observed in Fig. 4(d), it is plausible that the film interfaces may behave as magnetically inactive or *dead* layers. This interpretation is consistent with well-established observations in related complex oxide systems. For example, Porter *et al.* reported magnetic *dead* layers of ~0.8–1.5 nm in $La_{0.7}Sr_{0.3}MnO_3$ (LSMO) films grown on STO substrates, depending on substrate type and film thickness.[52] Similar interfacial magnetic suppression has also been observed in SRO thin films. Horiuchi *et al.* recently described a ~3 nm region near the SRO/STO interface as a *dead* layer characterized by reduced magnetization and conductivity, although the microscopic origin of this behavior was not discussed in detail.[53] Other studies have also reported that near-interface regions in SRO exhibit diminished ferromagnetism or even non-magnetic behavior associated with disorder, stoichiometric deviations, or strain effects.[54,55] In manganite heterostructures, the emergence of such magnetically *dead* layers has been linked to a combination of structural distortions, orbital reconstruction, oxygen vacancies, and interfacial strain.[56–59] Similar mechanisms may also play a role in the interfacial magnetic suppression observed in ruthenate films.

In the present case, however, modeling the interfaces as completely non-magnetic did not yield satisfactory results (supplementary material, Sec. S7). Such a model significantly altered the oscillation periodicity of the reflectivity curves, leading to unphysical estimates of the film thickness. These discrepancies indicate that, although the interfacial magnetization is strongly reduced, it does not vanish entirely. A more physically consistent explanation is that the PMA near the interfaces is stronger than in the film bulk, constraining the local magnetization to remain predominantly OP and thus reducing its IP projection detected by PNR. In SRO, such an interfacial anisotropy enhancement is more appropriately understood in terms of the coupled Ru–O electronic network than as a purely Ru-centered effect. Recent work has highlighted the role of ligand-driven anisotropy in SRO, showing that the orbital response of the ligand O 2*p* states, induced through hybridization with Ru 4*d* states, plays a key role in determining the magnetic anisotropy, while neutron diffraction studies on bulk single crystals have shown that oxygen carries a non-negligible fraction of the total magnetic moment, on the order of ~ 30%.[46,47] Within this framework, interfacial Ru deficiency and non-stoichiometry may alter the local Ru–O hybridization and thereby enhance the interfacial anisotropy while reducing the in-plane magnetic projection detected by PNR. Accordingly, the refined model incorporating partially magnetized interfacial regions due to enhanced OP anisotropy reproduces the experimental data more accurately.

This finding highlights that Ru deficiency and local anisotropy variations at the interfaces play a central role in suppressing the IP magnetization, while the overall ferromagnetic integrity of the SRO film remains preserved. Importantly, these results show that the reduced interfacial magnetization often inferred in Ru-deficient SRO does not originate from magnetically *dead* layers, but rather from strongly anisotropic interfacial magnetism, plausibly linked to local modifications of the Ru–O electronic structure.

IV. CONCLUSION

In summary, a comprehensive set of complementary techniques establishes that SRO thin films grown by RF-HOPS are intrinsically Ru-deficient, with an enhanced deficiency at the interfaces and a finite deficiency extending throughout the film bulk. This non-stoichiometry strongly suppresses coherent electronic transport and reduces the saturation magnetization without significantly affecting T_{Curie}, placing Ru-deficient SRO in a regime consistent with ferromagnetic insulator-like behavior.

Depth- and lateral-resolved magnetic probes indicate that the reduced magnetization at the interfaces does not arise from fully magnetically *dead* layers. Instead, the interfacial regions remain ferromagnetic and show a reduced in-plane magnetic projection consistent with enhanced PMA that keeps the local magnetization predominantly out of plane. As a result, the magnetic response of

28 May 2026 14:04:25

© Author(s) 2026

Ru-deficient SRO films is more consistently understood in terms of anisotropy gradients and partial canting than as a simple loss of magnetic order.

These findings highlight Ru deficiency as an effective control parameter for simultaneously tuning transport, magnetization, and anisotropy in correlated oxide thin films. These results show that defect and interface engineering provide effective routes to modulate interfacial magnetism beyond simple *dead* layer scenarios, with direct relevance for the design of oxide heterostructures with tailored magnetic functionalities.

SUPPLEMENTARY MATERIAL

The supplementary material provides additional structural, magnetic, and neutron-scattering analysis, including complementary characterization data, model comparisons, and quantitative estimates supporting the main text.

ACKNOWLEDGMENTS

The authors thank F. Gossen, L. Kibkalo, and B. Schmitz for their technical assistance. The authors thank T. Denneulin, L. Jin, A. Kovács, O. Petracic, and U. Poppe for the discussions. This work was sponsored by the Tasso Springer Fellowship provided by JCNS. This research used resources at the Spallation Neutron Source, a DOE Office of Science User Facility operated by the Oak Ridge National Laboratory. The beam time was allocated to MAGREF under Proposal No. IPTS-32745.1.

AUTHOR DECLARATIONS

Conflict of Interest

The authors have no conflicts to disclose.

Author Contributions

V. A. de Oliveira Lima: Conceptualization (lead); Data curation (lead); Formal analysis (lead); Investigation (lead); Methodology (lead); Visualization (lead); Writing – original draft (lead); Writing – review & editing (lead). **S. Nandi**: Conceptualization (equal); Supervision (equal); Writing – review & editing (equal). **T. Brückel**: Supervision (equal); Writing – review & editing (equal). **M. I. Faley**: Data curation (equal); Investigation (equal); Methodology (equal); Writing – review & editing (equal). **O. Concepción**: Investigation (equal); Writing – review & editing (equal). **A. Qdemat**: Data curation (equal); Formal analysis (equal); Investigation (equal); Methodology (equal); Writing – review & editing (equal). **H. Ambaye**: Data curation (equal); Investigation (equal); **V. Lauter**: Data curation (equal); Investigation (equal); Methodology (equal); Supervision (equal); Writing – review & editing (equal). **M. Radovic**: Formal analysis (equal); Writing – review & editing (equal). **A. Singh**: Investigation (equal); Writing – review & editing (equal). **E. Kentzinger**: Data curation (equal); Formal analysis (equal); Investigation (equal); Methodology (equal); Supervision (equal); Writing – review & editing (equal). **C. Bednarski-Meinke**: Data curation (equal); Investigation (equal); Supervision (equal); Writing – review & editing (equal).

DATA AVAILABILITY

The data that support the findings of this study are available within the article and its supplementary material.

REFERENCES

[1] M. Cuoco and A. Di Bernardo, APL Mater. **10**, 090902 (2022).
[2] Y. Gu, Q. Wang, W. Hu, W. Liu, Z. Zhang, F. Pan, and C. Song, J. Phys. D: Appl. Phys. **55**, 233001 (2022).
[3] Y. K. Wakabayashi, M. Kobayashi, Y. Takeda, K. Takiguchi, H. Irie, S.-i. Fujimori, T. Takeda, R. Okano, Y. Krockenberger, Y. Taniyasu, and H. Yamamoto, Phys. Rev. Mater. **5**, 124403 (2021).
[4] V. A. de Oliveira Lima, M. Faley, O. Concepción, S. Nandi, P. Prakash, M. H. Hamed, E. Kentzinger, T. Brueckel, and C. Bednarski-Meinke, Phys. Scr. **100**, 075985 (2025).
[5] K. Takiguchi, Y. K. Wakabayashi, H. Irie, Y. Krockenberger, T. Otsuka, H. Sawada, S. A. Nikolaev, H. Das, M. Tanaka, Y. Taniyasu, and H. Yamamoto, Nat. Commun. **11**, 4969 (2020).
[6] H. Huang, S.-J. Lee, B. Kim, B. Sohn, C. Kim, C.-C. Kao, and J.-S. Lee, ACS Appl. Mater. Interfaces **12**, 37757 (2020).
[7] X. Zheng, Z. Lu, B. Lao, S. Peng, K. Wu, S. Li, R.-W. Li, M. Radovic, and Z. Wang, Phys. Rev. Mater. **9**, 074403 (2025).
[8] Y. Chen, D. L. Bergman, and A. A. Burkov, Phys. Rev. B **88**, 125110 (2013).
[9] A. F. Marshall, L. Klein, J. S. Dodge, C. H. Ahn, J. W. Reiner, L. Mieville, L. Antagonazza, A. Kapitulnik, T. H. Geballe, and M. R. Beasley, J. Appl. Phys. **85**, 4131 (1999).
[10] B. Sohn, E. Lee, S. Y. Park, W. Kyung, J. Hwang, J. D. Denlinger, M. Kim, D. Kim, B. Kim, H. Ryu *et al.*, Nat. Mater. **20**, 1643 (2021).
[11] Y. K. Wakabayashi, S. Kaneta-Takada, Y. Krockenberger, Y. Taniyasu, and H. Yamamoto, ACS Appl. Electron. Mater. **3**, 2712 (2021).
[12] J. Xia, W. Siemons, G. Koster, M. R. Beasley, and A. Kapitulnik, Phys. Rev. B **79**, 140407 (2009).
[13] D. Toyota, I. Ohkubo, H. Kumigashira, M. Oshima, T. Ohnishi, M. Lippmaa, M. Takizawa, A. Fujimori, K. Ono, M. Kawasaki *et al.*, Appl. Phys. Lett. **87**, 162508 (2005).
[14] J. Zhang, Z. Jiang, H. Huang, Z. Shan, L. Wang, J. Wang, Q. Huang, Z. Fu, and Y. Lu, Appl. Phys. Lett. **122**, 062406 (2023).
[15] Y. K. Wakabayashi, S. Kaneta-Takada, Y. Krockenberger, K. Takiguchi, S. Ohya, M. Tanaka, Y. Taniyasu, and H. Yamamoto, AIP Adv. **11**, 035226 (2021).
[16] G. Koster, L. Klein, W. Siemons, G. Rijnders, J. S. Dodge, C.-B. Eom, D. H. A. Blank, and M. R. Beasley, Rev. Mod. Phys. **84**, 253 (2012).
[17] M. Młynarczyk, "Physicochemical properties of the $Sr_{1-x}Ca_xRuO_3$ thin films," Ph.D. thesis, Jagiellonian University, 2013.
[18] M. Mlynarczyk, K. Szot, A. Petraru, U. Poppe, U. Breuer, R. Waser, and K. Tomala, J. Appl. Phys. **101**, 023701 (2007).
[19] W. Siemons, G. Koster, A. Vailionis, H. Yamamoto, D. H. A. Blank, and M. R. Beasley, Phys. Rev. B **76**, 075126 (2007).
[20] J. Hoppler, J. Stahn, H. Bouyanfif, V. K. Malik, B. D. Patterson, P. R. Willmott, G. Cristiani, H.-U. Habermeier, and C. Bernhard, Phys. Rev. B **78**, 134111 (2008).
[21] Z. Zhang, P. Qian, X. Yang, B. Wu, H. L. Cai, F. M. Zhang, and X. S. Wu, Sci. Rep. **12**, 2499 (2022).
[22] E. McCalla, J. Walter, and C. Leighton, Chem. Mater. **28**, 7973 (2016).
[23] F. Sánchez, C. Ocal, and J. Fontcuberta, Chem. Soc. Rev. **43**, 2272 (2014).
[24] U. Poppe, N. Klein, U. Dähne, H. Soltner, C. Jia, B. Kabius, K. Urban, A. Lubig, K. Schmidt, S. Hensen *et al.*, J. Appl. Phys. **71**, 5572 (1992).
[25] C. L. Jia, J. R. Contreras, U. Poppe, H. Kohlstedt, R. Waser, and K. Urban, J. Appl. Phys. **92**, 101 (2002).

28 May 2026 14:04:25

© Author(s) 2026

[26]M. I. Faley, *Epitaxial Oxide Heterostructures for Ultimate high-T_c Quantum Interferometers in Applications of High-T_c Superconductivity* (InTech, Rijeka, 2011), pp. 147–176.
[27]V. Lauter, H. Ambaye, R. Goyette, W.-T. Hal Lee, and A. Parizzi, Physica B **404**, 2543 (2009).
[28]R. A. Rao, Q. Gan, and C.-B. Eom, Appl. Phys. Lett. **71**, 1171 (1997).
[29]Q. Gan, R. A. Rao, and C. B. Eom, Appl. Phys. Lett. **70**, 1962 (1997).
[30]W. Wang, L. Li, J. Liu, B. Chen, Y. Ji, J. Wang, G. Cheng, Y. Lu, G. Rijnders, G. Koster *et al.*, npj Quantum Mater. **5**, 73 (2020).
[31]N. Iles, F. Finocchi, and K. D. Khodja, J. Phys. Condens. Matter. **22**, 305001 (2010).
[32]J. C. Jiang, W. Tian, X. Q. Pan, Q. Gan, and C. B. Eom, Appl. Phys. Lett. **72**, 2963 (1998).
[33]A. Glavic and M. Björck, J. Appl. Crystallogr. **55**, 1063 (2022).
[34]G. Rijnders, D. H. A. Blank, J. Choi, and C.-B. Eom, Appl. Phys. Lett. **84**, 505 (2004).
[35]M. Nakahara, S. Tsunekawa, K. Watanabe, T. Arai, T. Yunogami, and K. Kuroki, J. Vac. Sci. Technol., B **19**, 2133 (2001).
[36]Y. Z. Yoo, O. Chmaissem, S. Kolesnik, B. Dabrowski, M. Maxwell, C. W. Kimball, L. McAnelly, M. Haji-Sheikh, and A. P. Genis, J. Appl. Phys. **97**, 103525 (2005).
[37]M. Zahradník, K. Uhlířová, T. Maroutian, G. Kurij, G. Agnus, M. Veis, and P. Lecoeur, Mater. Des. **187**, 108390 (2020).
[38]R. Palai, H. Huhtinen, J. F. Scott, and R. S. Katiyar, Phys. Rev. B **79**, 104413 (2009).
[39]A. S. Goossens, M. Leiviskä, and T. Banerjee, Front. Nanotechnol. **3**, 680468 (2021).
[40]M. Ziese, I. Vrejoiu, and D. Hesse, Phys. Rev. B **81**, 184418 (2010).
[41]V. Lauter-Pasyuk, Collect. SFN **7**, 221 (2007).
[42]J. Daillant and A. Gibaud, *X-ray and Neutron Reflectivity: Principles and Applications* (Springer, 2008), Vol. 770.
[43]B. P. Toperverg and H. Zabel, *Experimental Methods in the Physical Sciences* (Elsevier, 2015), Vol. 48, pp. 339–434.
[44]V. Lauter, K. Wang, T. Mewes, A. Glavic, B. Toperverg, M. Ahmadi, B. Assaf, B. Hu, M. Li, X. Liu *et al.*, Rev. Sci. Instrum. **93**, 103903 (2022).
[45]R. Dronskowski, T. Brückel, H. Kohlmann, M. Avdeev, A. Houben, M. Meven, M. Hofmann, T. Kamiyama, M. Zobel, W. Schweika *et al.*, Z. Kristallogr. Cryst. Mater. **239**, 139 (2024).
[46]Y. K. Wakabayashi, M. Kobayashi, Y. Seki, Y. Kotani, T. Ohkochi, K. Yamagami, M. Kitamura, Y. Taniyasu, Y. Krockenberger, and H. Yamamoto, APL Mater. **12**, 041119 (2024).
[47]S. Kunkemöller, K. Jenni, D. Gorkov, A. Stunault, S. Streltsov, and M. Braden, Phys. Rev. B **100**, 054413 (2019).
[48]Y. Yoneda, Phys. Rev. **131**, 2010 (1963).
[49]H. J. C. Lauter, V. Lauter, and B. P. Toperverg, *Polymer Science: A Comprehensive Reference* (Elsevier, 2012), Vols. 1–10, pp. 411–432.
[50]E. Kentzinger, U. Rücker, B. Toperverg, F. Ott, and T. Brückel, Phys. Rev. B **77**, 104435 (2008).
[51]F. Ott and S. Kozhevnikov, J. Appl. Crystallogr. **44**, 359 (2011).
[52]S. B. Porter, M. Venkatesan, P. Dunne, B. Doudin, K. Rode, and J. M. D. Coey, IEEE Trans. Magn. **53**, 1 (2017).
[53]H. Horiuchi, Y. Araki, Y. K. Wakabayashi, J. Ieda, M. Yamanouchi, Y. Sato, S. Kaneta-Takada, Y. Taniyasu, H. Yamamoto, Y. Krockenberger *et al.*, Adv. Mater. **37**, 2416091 (2025).
[54]Z. Ali, Z. Wang, A. O'Hara, M. Saghayezhian, D. Shin, Y. Zhu, S. T. Pantelides, and J. Zhang, Phys. Rev. B **105**, 054429 (2022).
[55]E. Falsetti, A. Kalaboukhov, A. Nucara, M. Ortolani, M. Corasaniti, L. Baldassarre, P. Roy, and P. Calvani, Sci. Rep. **8**, 15217 (2018).
[56]D. Pesquera, G. Herranz, A. Barla, E. Pellegrin, F. Bondino, E. Magnano, F. Sánchez, and J. Fontcuberta, Nat. Commun. **3**, 1189 (2012).
[57]R. Trappen, *Depth Dependent Atomic Valence Determination in $La_{0.7}Sr_{0.3}MnO_3$ Thin Films Using Synchrotron Techniques* (West Virginia University, 2019).
[58]V. A. de Oliveira Lima, "Propriedades eletrônicas e magnéticas de filmes ultrafinos de $La_{0.67}Sr_{0.33}MnO_3$," M.S. thesis, Universidade Federal de Campina Grande, 2021.
[59]D. Schumacher, A. Steffen, J. Voigt, J. Schubert, T. Brückel, H. Ambaye, and V. Lauter, Phys. Rev. B **88**, 144427 (2013).

28 May 2026 14:04:25

© Author(s) 2026